nature communications

Article

https://doi.org/10.1038/s41467-025-61185-3

Facilitating carrier kinetics in ultrathin porous carbon nitride through shear-repair strategy for peroxymonosulfate-assisted water purification

Received: 21 November 2024

Accepted: 12 June 2025

Published online: 01 July 2025

Check for updates

Hao Liu[1,6], Bin Yang[1,6] ✉, Guangfu Liao[2], Baoyu Huang[3], Jun Li[4] ✉, Raul D. Rodriguez[5] & Xin Jia[1] ✉

Achieving high specific surface area (HSSA) in graphitic carbon nitride (g-C_3N_4) severely depolymerizes the molecular chain structure, resulting in sluggish carrier kinetic behaviors and thus moderated water purification performance in photocatalytic peroxymonosulfate (PMS) activation system. Herein, we report a versatile shear-repair strategy for fabricating ultrathin porous g-C_3N_4 nanosheets with a thickness of 1.5 nm, HSSA (138.5 m^2 g^{-1}), and highly polymerized molecular chains. This strategy accelerates exciton dissociation and charge carrier separation, with the exciton binding energy decreasing from 65.7 to 47.5 meV. Crucially, the electron-donating pollutant and electron-withdrawing PMS generate a microelectric field at the g-C_3N_4 surface that activates PMS to generate $^1O_2$ sustainably. Consequently, our catalyst exhibits an exceptional imidacloprid (IMD) removal performance with a rate constant of 0.405 min^{-1} and remarkable PMS utilization efficiency (90% within 15 min). Moreover, under real conditions of sunlight irradiation, we observe an outstanding pollutants' removal efficiency with a near-100% degradation rate over 20 days of continuous operation. Our work emphasizes the feasibility of synergistic molecular-level structural engineering for refining carrier kinetic behaviors in high-performance photocatalyst design.

Polymeric graphitic carbon nitride (g-C_3N_4) presents a promising candidate as a star photocatalyst owning to its robust stability, tunable electronic structure and facile fabrication[1,2]. Since the pioneering work reported by Wang and co-workers in 2008[3], g-C_3N_4 has been widely employed in various photocatalytic energy conversion and environmental remediation fields in the following decades, especially demonstrating enormous application prospects for removing persistent pollutants in photocatalytic peroxymonosulfate (PC-PMS) activation system[4–6]. Nevertheless, the pristine g-C_3N_4 is plagued by ultralow specific surface area and incompletely polymerized molecular chains structure, leading to sluggish exciton dissociation and severe in-plane photogenerated carriers recombination, which seriously restricts the effective photocatalysis[7,8]. Therefore, designing a g-C_3N_4 with a high specific surface area (HSSA) and highly polymerized molecular chains to optimize carrier kinetic behaviors to address these challenges is essential.

[1]School of Chemistry and Chemical Engineering/State Key Laboratory Incubation Base for Green Processing of Chemical Engineering, Shihezi University, Shihezi, China. [2]College of Material Engineering, Fujian Agriculture and Forestry University, Fuzhou, P. R. China. [3]Hunan Provincial Key Laboratory of Environmental Catalysis & Waste Recycling, College of Materials and Chemical Engineering, Hunan Institute of Engineering, Xiangtan, China. [4]School of Chemical Engineering, Henan Institute of Advanced Technology, Zhengzhou University, Zhengzhou, P.R. China. [5]Tomsk Polytechnic University, 30 Lenin Avenue, Tomsk, Russia. [6]These authors contributed equally: Hao Liu, Bin Yang. ✉e-mail: yangbin@shzu.edu.cn; junli2019@zzu.edu.cn; jiaxin@shzu.edu.cn

Ultrathin porous g-C_3N_4 nanosheets with HSSA are desirable for photocatalysis due to their larger active space for the matter diffusion and conversion as well as shorter charge carriers' transfer distance[9,10]. Recently, various strategies have been reported for synthesizing ultrathin porous g-C_3N_4 nanosheets, among which the shear of the thermal active atmospheres is widely recognized as the most effective method[11–13]. Since Liu and co-workers first proposed the cutting bulk g-C_3N_4 into ultrathin porous architecture in thermal air[14,15], numerous researchers have subsequently attempted to prepare ultrathin porous g-C_3N_4 nanosheets using the shear of various thermal active atmospheres like ammonia[16], hydrogen[17], oxygen[18], and water vapor[19], resulting in nanostructured g-C_3N_4 with exceptional photocatalytic performance. However, this process inevitably exacerbates the intrinsic incomplete polymerization of the heptazine-based molecular chains by breaking the imine linkages[20,21], leading to sluggish exciton dissociation, arduous in-plane charge transfer, deep charge trapping states and severe bulk electron-hole pair's recombination[22]. Recent works have explored accelerating the in-plane charge transport of g-C_3N_4 by inducing more complete polymerization of the heptazine-based molecular chains. For instance, Zhang et al. fragmented g-C_3N_4 into smaller pieces, followed by subjecting it to a directed healing process to boost charge dynamics[23]. Li et al. constructed a highly crystalline g-C_3N_4 through a molten salt-assisted in-plane "stitching" and interlayer "cutting" to achieve rapid charge transport and separation[24]. Inspired by these works, we envisage that precisely mending the incomplete polymerized molecular chains of ultrathin porous g-C_3N_4 nanosheets maintaining HSSA would dramatically improve the carrier kinetic behaviors to boost the photocatalytic PMS activation.

Following the above hypothesis, ultrathin porous g-C_3N_4 nanosheets with HSSA and highly polymerized molecular chains were fabricated by the versatile shear-repair strategy under thermally active and subsequently inert atmospheres. The as-prepared photocatalyst exhibited lower exciton dissociation energy, higher charge carrier separation, and transport efficiency along the in-plane molecular chains. Importantly, a microelectric field at the g-C_3N_4 surface induced by the potential difference between the electron-donating pollutant and electron-withdrawing PMS was successfully constructed, which further boosted the spatial separation of the photogenerated carriers while efficiently activating PMS to sustainably generate $^1O_2$ for degrading and mineralizing various persistent pollutants even under harsh environmental conditions. Moreover, under real conditions of sunlight irradiation, the photocatalyst consistently maintained near-100% pollutant' removal efficiency during 20 days of operation in custom-built continuous photo-flow device. This work also emphasizes that the maintenance of highly polymerized molecular chains is more crucial for optimizing carrier kinetic behaviors than simply increasing the specific surface area of photocatalyst. These insights push our way forward in the rational design of polymer semiconductors.

Results

Materials synthesis and characterizations

A schematic diagram illustrates the fabrication of the photocatalysts and the corresponding molecular-level structural regulation (Fig. 1a). First, the bulk g-C_3N_4 with incomplete polymerization structure (CN) originated from the thermal polymerization of urea was stripped into ultrathin porous nanosheets possessing HSSA (ACN) by the shear of thermal NH_3 atmosphere. Computational simulations showed that NH_3 molecules preferentially adsorb and react with imine linkages connecting adjacent heptazine units (Fig. 1b, c). This reaction broken the heptazine chains, led to the generation of abundant amino groups and exacerbated the incomplete polymerization of g-C_3N_4. However, the higher formation energy (E_r) of nitrogen atoms in imine linkages than in amino groups (Fig. 1d), indicated a tendency for amino groups to convert back into imine linkages through repolymerization[25]. Consequently, the broken heptazine chains in ACN can be further precisely mended by thermal repolymerization among amino groups, yielding ultrathin porous g-C_3N_4 nanosheets with HSSA and highly polymerized heptazine chains (NACN). Furthermore, the rationality of the experimental design was demonstrated by reversing the order of the shear and repair steps. Briefly, the bulk g-C_3N_4 with highly polymerized heptazine chains (NCN) was synthesized via directly mending CN by thermal repolymerization under N_2 atmosphere. Subsequently, the ANCN was obtained by cutting NCN in thermal NH_3 atmosphere (see Methods).

The morphology and structure of these catalysts were elucidated using scanning electron microscopy (SEM) (SEM, Supplementary Fig. 1), high-resolution transmission electron microscopy (HRTEM) (HRTEM, Supplementary Fig. 2), and atomic force microscopy (AFM) (AFM) images (Fig. 1e). These analyses revealed the layered structure of bulk CN with a thickness of about 4.7 nm. After subjecting CN to the shear of the thermal NH_3 atmosphere, the resulting ACN was converted into ultrathin porous nanosheets with a thickness of 2.1 nm. The subsequent thermal repolymerization process yielded NACN, which inherited the ultrathin porous properties of ACN, and the thickness was maintained at 1.5 nm. Interestingly, there were only minor changes in morphology and thickness of NCN subjected to direct thermal repolymerization (see NCN in Fig. 1e). Subsequent treatment of NCN in a thermal NH_3 atmosphere produced ANCN with similar morphology and thickness to NACN. Meanwhile, the volume change sequence of the samples with the same mass followed the order: CN ≈ NCN < ACN ≈ ANCN ≈ NACN (Supplementary Fig. 1f). These results implied that the morphological changes and volume expansion of the prepared samples primarily arose from the shear of thermal NH_3 atmosphere rather than the repair of thermal repolymerization. The specific surface area and pore structure of the catalysts were investigated by N_2 adsorption-desorption measurements. As presented in Fig. 1f and Supplementary Table 1, the Brunauer-Emmett-Teller surface area were determined to be 128.46, 138.51, and 134.57 $m^2 g^{-1}$ for ACN, NACN, and ANCN, respectively, which were around two-fold than that of CN (62.59 $m^2 g^{-1}$) and NCN (71.30 $m^2 g^{-1}$). The pore size distribution results in Fig. 1g and Supplementary Table 1 indicated that the pore volume of ACN (0.43 $cm^3 g^{-1}$), NACN (0.41 $cm^3 g^{-1}$), and ANCN (0.38 $cm^3 g^{-1}$) were larger than those of CN (0.18 $cm^3 g^{-1}$) and NCN (0.25 $cm^3 g^{-1}$), suggesting the shear process introduced larger pore volume and richer pore structure in g-C_3N_4[26].

Above results collectively confirmed that the shear of the thermal NH_3 atmosphere and the repair of thermal repolymerization contributed differently to the catalysts' properties. The former primarily imparted ultrathin porous properties to g-C_3N_4 but exacerbated incomplete polymerization of heptazine chains by cutting imine linkages, while the latter mainly mended the broken heptazine chains at the molecular level.

Molecular-level structure characterizations

We conducted a detailed characterization of the catalysts obtained to investigate the molecular level structural changes induced by the shear and repair. The similar *X*-ray diffraction (XRD) patterns and Fourier transform infrared (FTIR) spectra (Fig. 2a, b) indicated that the basic structure of melon-type g-C_3N_4 was well preserved in prepared samples[27–31]. The *X*-ray photoelectron spectroscopy (XPS) and elemental analysis (EA) (Fig. 2c and Supplementary Tables 2, 3) revealed that the C/N atomic ratio of CN was higher than that of ACN and ANCN but lower than NACN and NCN. Notably, we also detected the NH_3 in exhaust gases in the thermal repair process (Supplementary Fig. 4). These indicated that the shear process introduced more nitrogen atoms into the g-C_3N_4 framework due to the formation of ample amino groups. In contrast, the repair process led to partial nitrogen atoms loss through the repolymerization among amino groups to release

https://doi.org/10.1038/s41467-025-61185-3

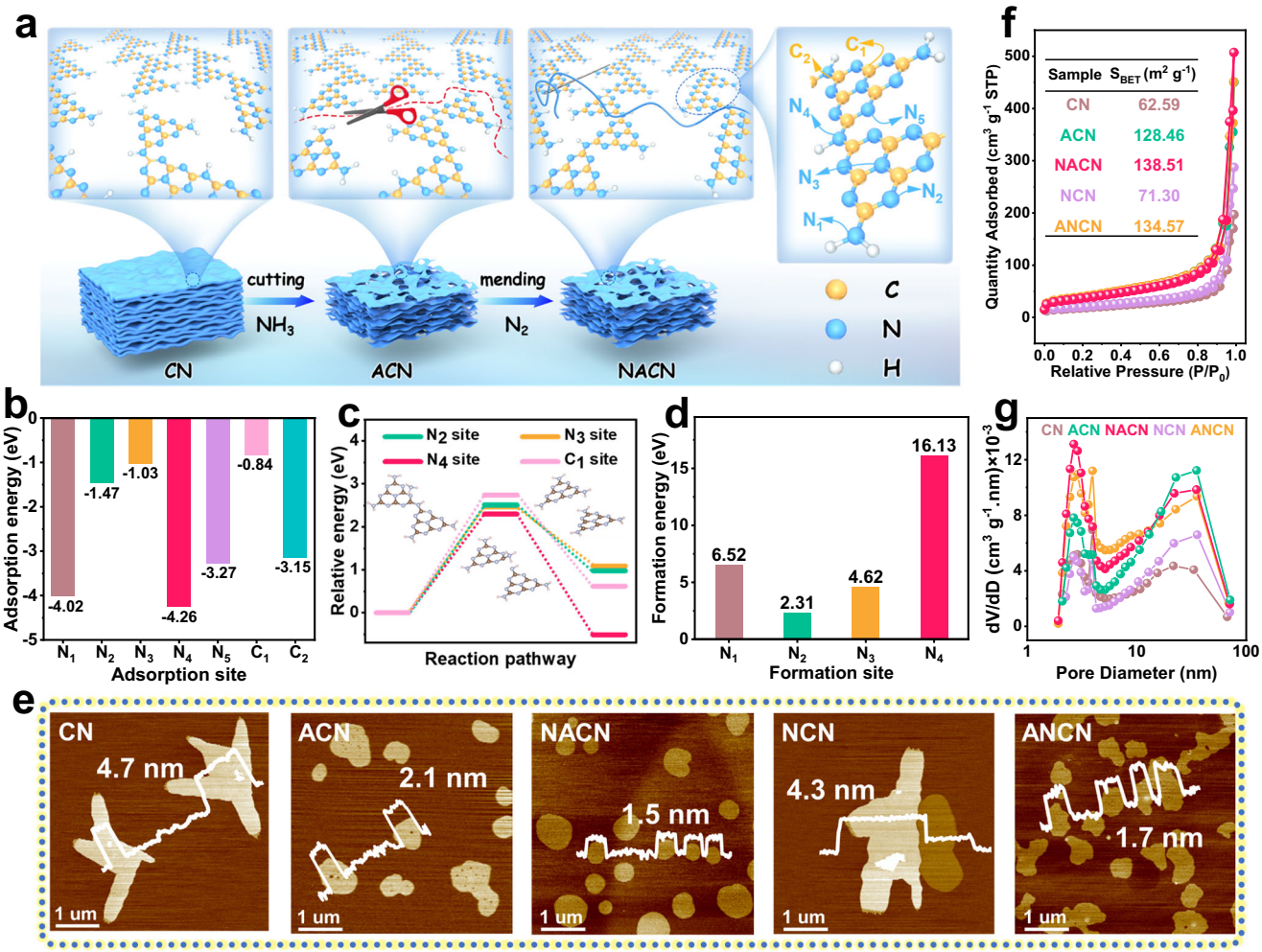

Fig. 1 | Synthetic illustration and morphology characterizations. a Schematic illustration of the synthesis process of photocatalysts; **b** Adsorption energy of NH_3; **c** The energy change of the NH_3 reaction process; **d** The formation energy of nitrogen atoms at different sites; **e** AFM images of prepared samples; **f** N_2 adsorption-desorption isotherms curves, and **g** pore size distribution curves of prepared samples. Source data are provided as a Source Data file.

NH_3. In the C 1*s* spectra, there were two peaks at 288.2 and 284.8 eV (Fig. 2d, Supplementary Table 4), corresponding to sp^2 hybridized carbon (N-C = N) and amorphous carbon (C-C/C = C), respectively[32]. The *N* 1*s* spectra (Fig. 2e) were deconvoluted into four peaks at 401.3 eV (tertiary nitrogen, N-$(C)_3$), 400.5 eV (imine group, 2C-NH), 399.5 eV (amino group, C-NH_2) and 398.6 eV (sp^2-coordinated nitrogen, C-N = C), respectively[33]. Significantly, the C-N = C/N-$(C)_3$ component ratio of all samples remained nearly unchanged (Supplementary Table 5), indicating that neither the shear nor the repair processes compromised the completeness of heptazine units. Additionally, a lower component ratio of 2C-NH/N-$(C)_3$ was observed in ACN (1.04) and ANCN (1.05) compared to CN (1.15), while NCN (1.19) and NACN (1.18) showed higher ratios than CN. These results confirmed that the shear process generated abundant amino groups by breaking imine linkages, while the repair process mended these linkages by the repolymerization among amino groups. Furthermore, solid-state ^{13}C NMR spectra (Fig. 2f, Supplementary Table 6) showed two prominent peaks at 155.8 and 164.5 ppm, corresponding to the N-C = N (C2) and the C-NH_x (C1), respectively[34]. The C1/C2 ratio of CN (2.378) was lower than ACN (2.424) and ANCN (2.396), but higher than NCN (2.373) and NACN (2.314), further confirming the roles of shear and repair engineering of the molecular structure[35].

X-ray absorption near-edge structure spectroscopy was used to further elucidate the chemical state and coordination environment changes induced by the shear and repair processes. With looking into the *C* K-edge spectra (Fig. 2g), three peaks at 285.9, 288.5 (C1), and 294.6 eV (C2) were derived from the structural defects, in-plane π^* N − C = N and σ^* N − C − N coordination, respectively[36]. Compared with CN counterpart, the peak intensities of C1 and C2 in ACN were significantly weaker, which was attributed to the in-plane structural disorganization arose by the broken molecular chains[37]. This was consistent with the shear process broken the imine linkages to generate copious amino groups, resulting in a large amount of in-plane structural defects. Notably, the absorption edge of NACN was similar to that of CN, suggesting the surface structure defects in ACN were mended via the repolymerization process among amino groups by forming new imine linkages.

In the *N* K-edge spectra (Fig. 2h), two peaks at 402.8 and 405.9 eV corresponded to the N1 site of the C − N = C coordination structure and the N3 site of imine linkages (C-N-C), respectively. The N2 site at 404.8 eV was due to the N 1*s* → π^* transition of graphitic nitrogen in the N−$(C)_3$ coordination[38]. The intensity of the N3 peak in ACN was significantly lower than that of CN, directly demonstrating that the shear of thermal NH_3 atmosphere disruption of imine linkages. Moreover, the intensities of all three peaks of NACN were higher than those of CN and ACN. This was consistent with XPS and NMR results, confirming that the thermal repolymerization mended broken imine linkages to form intact heptazine chains of g-C_3N_4 with fewer defects[39]. Such intact heptazine chains could create efficient charge transfer channels for rapid charge transport in NACN, minimizing their recombination[40].

https://doi.org/10.1038/s41467-025-61185-3

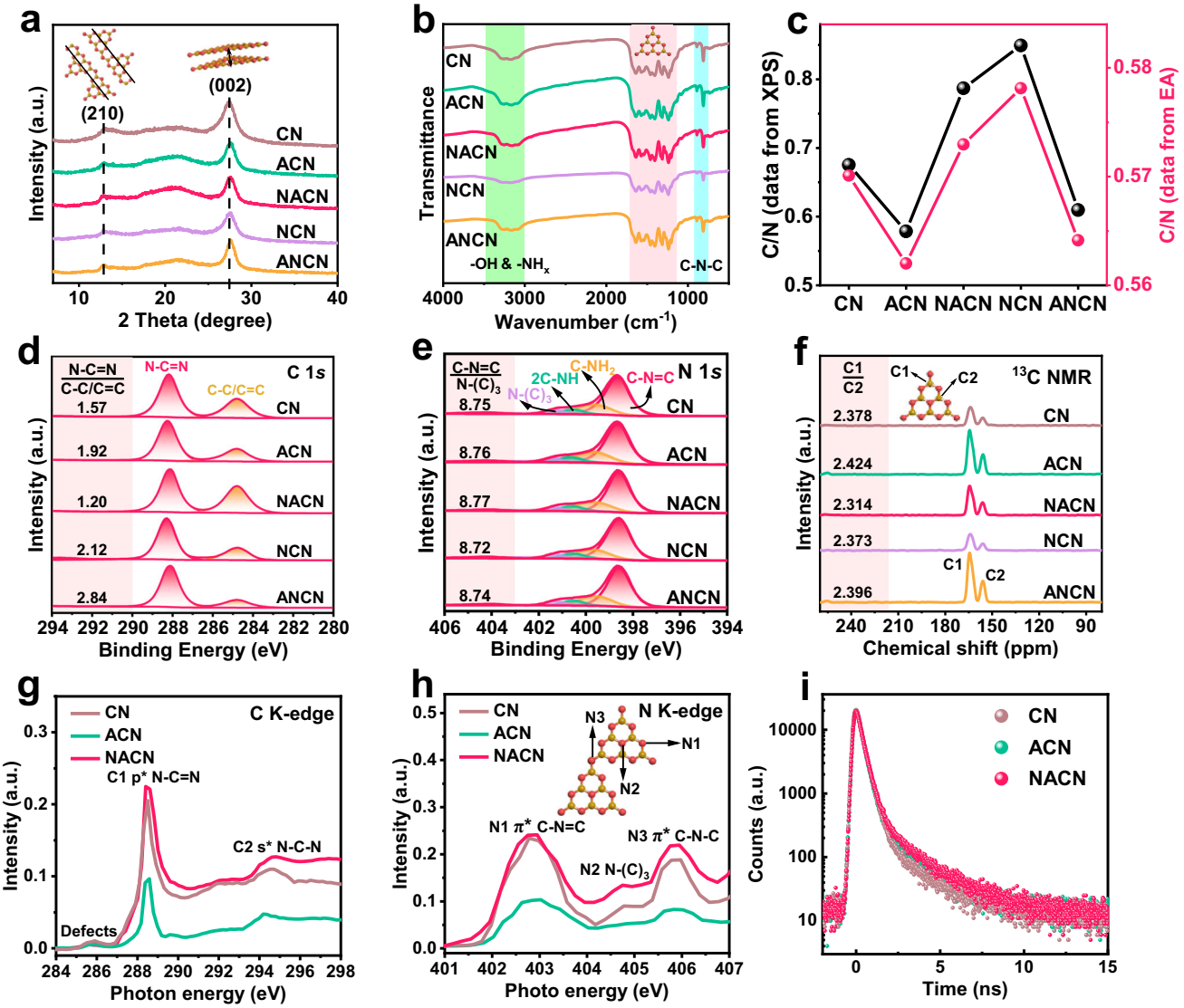

Fig. 2 | Structural characterizations of all catalysts. a XRD patterns and **b** FT-IR spectra of prepared samples; **c** C/N ratio from XPS and EA; **d** XPS spectra of C 1*s* and **e** N 1*s*; **f** Solid-state ^{13}C NMR spectrum; **g** C K-edge XANES spectra and **h** N K-edge XANES spectra; **i** PALS spectra of prepared samples. Source data are provided as a Source Data file.

To further identify and quantify the variations in structural defects induced by cutting and mending of imine linkages, positron annihilation lifetime spectroscopy (PALS) was executed to analyze the species and defect concentration in the prepared samples[41]. As shown in Fig. 2i and Supplementary Table 7, three lifetime components τ_1, τ_2, and τ_3 were obtained from the PALS analysis. The shortest τ_1 was assigned to small-size defects exiting in the bulk, while the longest τ_3 was assigned to the positron annihilation in the pores. Both these two defects are generally beneficial for charge carrier kinetic[42]. The τ_2 component originated from larger surface defects, which commonly acts as recombination centers for in-plane charges[43]. Additionally, the relative intensities of these lifetime components (I) represented the concentration of the corresponding defects[44]. The I_1 and I_3 intensities followed the order: CN < ACN < NACN, indicating a higher content of small-size defects and pore structures in NACN. Moreover, the I_2 of NACN was lower than that of ACN, proving the repair process can mend surface structure defects by forming new imine linkages. These systematic characterizations confirmed the successful synthesis of the NACN photocatalyst with HSSA and highly polymerized molecular chains via shear and repair engineering.

Modulation of carrier kinetic behaviors

UV-Vis diffuse reflectance spectra of the samples (Fig. 3a) showed the optical absorption band edges of photocatalysts had only minor differences, indicating they had comparable optical absorption capabilities[45]. Additionally, the energy band structures of the samples were also determined (Supplementary Fig. 5). To understand the exciton dissociation kinetics, we conducted temperature-dependent photoluminescence (PL) spectroscopy. Excitons, formed due to the strong Coulomb interactions between electrons and holes, can limit charge separation, with the exciton binding energy (E_b) representing the energy required to dissociate excitons into free carriers. Therefore, weakening the exciton effect to promote carrier generation was crucial for optimizing charge separation and enhancing photocatalysis[46]. As observed in Supplementary Fig. 6, the PL intensity gradually decreased with the increasing temperature from 80 to 300 K, corresponding to a thermally activated nonradiative recombination process[47]. The E_b was calculated using nonlinear fitting and the Arrhenius equation (see Supplementary Discussion 5). As shown in Fig. 3b–d, the E_b of ACN was lower than that of CN, indicating that the HSSA reduced the probability of the exciton recombination due to the shortened carrier diffusion

https://doi.org/10.1038/s41467-025-61185-3

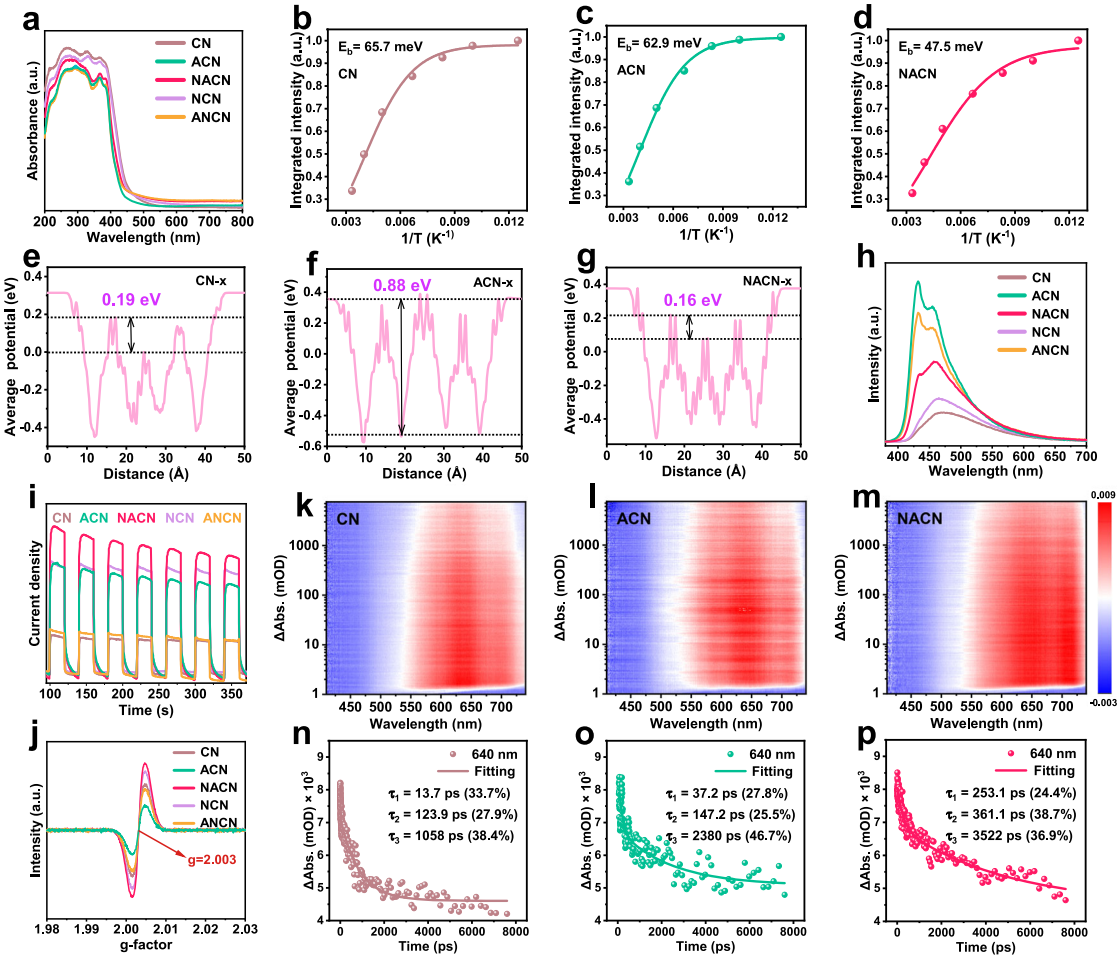

Fig. 3 | Carrier kinetic behaviors of prepared photocatalysts. a UV-Vis spectra of prepared samples; **b**–**d** Integrated PL emission intensity as a function of temperature ($\lambda_{excitation}$ = 370 nm) for CN, ACN, and NACN, respectively; **e**–**g** The calculated electrostatic potentials of samples along the x (molecular chain) direction; **h** The steady-state PL emission spectra ($\lambda_{excitation}$ = 370 nm); **i** Switching photocurrent responses of samples under λ ≥ 420 nm visible light; **j** ESR signal of prepared samples; **k**–**m** Time-dependent 3D contour plots of fs-TAS (pump laser: 330 nm); **n**–**p** TA decay kinetics probed at 640 nm. Source data are provided as a Source Data file.

distance. In contrast, the E_b of NACN was further decreased to 47.6 meV, which was attributed to the combination of HSSA and highly polymerized molecular chains facilitated the dissociation of excitons into free carriers.

Understanding how photogenerated carriers migrate to the catalyst surface is essential for modulating carrier kinetic behaviors. Therefore, the three-dimensional electrostatic potential of the samples was investigated by theoretical calculation. Specifically, the *x* and *y* directions were set as parallel and perpendicular to the heptazine-based molecular chains, respectively, and the *z* direction was perpendicular to the basal plane across the van der Waals force-mediated interlayers. As shown in Supplementary Fig. 7, the electrostatic potential in the *y* and *z* directions changed only slightly and was significantly higher than in the *x* direction (Fig. 3e–g). This indicated that photogenerated carriers preferentially transported along the x direction, parallel to the molecular chains. Furthermore, the electrostatic potential of ACN in the *x* direction was much higher than CN, directly demonstrating that the breakage of imine linkages resulted in frustrating structural defects that hinder charge transport along the molecular chains. In contrast, the electrostatic potential in the *x* direction decreased from 0.88 eV for ACN to 0.16 eV for NACN. This indicated that the repolymerization-driven repair of broken imine linkages facilitated the transport of photogenerated carriers to the photocatalyst surface along the molecular chains.

To further evaluate the carrier kinetic behaviors, we investigated the separation and migration efficiency of photogenerated carriers using steady-state PL spectroscopy[48]. As illustrated in Fig. 3h, ACN and ANCN showed a dramatic increase in PL emission compared to CN and NCN. This increase was attributed to the broken imine linkages, which aggravated the intrinsic radiative recombination of photogenerated charges. Moreover, NACN exhibited a weaker PL emission than ACN, indicating that repairing the broken imine linkages through repolymerization improved the charge separation process. This improvement in charge separation was further supported by photoelectrochemical measurements. NACN showed the largest instantaneous photocurrent density (Fig. 3i), the smallest electrochemical impedance radius (Supplementary Fig. 9), and the strongest electron spin resonance (ESR) signal (Fig. 3j). These results indicated the most efficient separation and migration efficiency of photogenerated carriers in NACN[49,50]. Furthermore, cyclic voltammetry was performed to determine the electrochemically active surface area (ECSA) based on the double-layer capacitance (C_{dl}). Notably, NACN showed the largest ECSA (Supplementary Fig. 10) due to the HSSA and highly polymerized molecular chains, suggesting that NACN possessed the highest density of photocatalytic active sites[51].

To visualize the accumulation of photogenerated carriers reaching the catalyst surface, we employed Kelvin probe force microscopy to probe the surface potential variations of the samples before and

after light illumination[52]. As shown in Supplementary Fig. 11, all samples showed an increased surface potential after light illumination, confirming the migration of photogenerated carriers from the photocatalyst bulk to the surface[53]. Impressively, the surface potential of ACN increased slightly after light illumination (from 18.7 to 20.1 mV) compared to CN (from 14.6 to 16.2 mV). This can be attributed to the competing effect of the shear process. Although the HSSA of ACN shortened the photogenerated carriers' migration distance, the structural defects formed by the breakage of the imine linkages increased charge recombination. These competing effects resulted in the unsatisfactory efficiency of photogenerated carriers' separation and migration for ACN. Notably, the surface potential of NACN increased more significantly (from 20.4 to 24.8 mv) than ACN due to the repair of broken imine linkages through repolymerization. By combining HSSA with highly polymerized molecular chains, NACN effectively promoted the migration and accumulation of photogenerated carriers at the catalyst surface.

Femtosecond transient absorption spectroscopy (fs-TAS) (fs-TAS, excited by 330 nm pump light) was applied to ulteriorly track the relaxation pathway of photogenerated carriers. As depicted in Fig. 3k–m, all samples immediately displayed a negative signal after pump excitation, followed by a positive signal appeared at 470 nm. The negative signal was assigned to the ground state bleaching, which reflected the population of photoexcited carriers at the conduction band (CB) edge[54]. The positive signal was attributed to excited-state absorption (ESA)[55]. Moreover, the ESA signal of NACN was stronger than that of CN and ACN, indicating a higher population of excited-state carriers in NACN[56]. Furthermore, all samples' transient absorption (TA) intensity decreased with increasing probe time (Supplementary Fig. 12), reflecting the relaxation process of CB electrons to trap at different depths. Simultaneously, the kinetic traces detected at the maximum fs-TA absorption around 640 nm were fitted to analyze the relaxation kinetics of excited-state carriers. The kinetics fitting results for CN revealed three decay lifetimes with $\tau_1 = 13.7$ ps (33.7%), $\tau_2 = 123.9$ ps (27.9%), and $\tau_3 = 1058$ ps (38.4%) (Fig. 3n), corresponding to shallow trapping states, deep trapping states, and the recombination of free photogenerated electrons and holes, respectively[57]. Notably, ACN exhibited a significantly prolonged τ_3 (2380 ps) with an increased contribution of 46.7% compared to CN (Fig. 3o), indicating the breakage of molecular chains exacerbated the recombination of photogenerated electrons and holes. In contrast, the NACN exhibited the longest lifetimes for τ_1 (253.1 ps, 24.4%) and τ_2 (361.1 ps, 38.7%), and the smallest contribution of τ_3 (3522 ps, 36.9%) (Fig. 3p). These results suggested that the combination of HSSA and highly polymerized molecular chains in NACN could induce long-lived shallow charge trapping, boost the photoelectron density and improve photocatalytic performance.

Evaluation of pollutants' removal activity

The accumulation of persistent pollutants, such as the neonicotinoid pesticide IMD, in natural water bodies severely threatens ecosystems and human health[58,59]. To evaluate the prepared samples' photocatalytic performance, we investigated their ability to degrade IMD and other refractory pollutants. Initially, we elucidated the sources of pollutants degradation driving forces in the PC-PMS system by performing IMD removal experiments in different catalytic systems. As illustrated in Supplementary Fig. 13, all samples showed negligible IMD adsorption (<2%) in 120 min without PMS and visible light. After the addition of PMS, NACN removed only 4% of IMD in 9 min under dark conditions (Fig. 4a). PMS alone cannot be directly activated by visible light while the NACN achieved 58% IMD removal with 9 min in the photocatalytic system. Notably, the NACN reached near-100% IMD removal within 9 min in the PC-PMS system, highlighting the effective photocatalytic PMS activation. The optimal concentrations of photocatalyst and PMS were set at 0.6 and 1.2 g L^{-1}, respectively (Supplementary Fig. 14). Additionally, all IMD degradation followed pseudo-first-order kinetics ($ln\frac{C}{C_0} = -k_{obs}t$), where C, C_0, and k_{obs} are the instantaneous and initial concentration of pollutants, as well as the degradation apparent rate constant, respectively. Subsequently, in order to optimize the synthesis conditions of photocatalysts, we evaluated the catalytic activity of ACN and NACN prepared through NH_3 shear and subsequent thermal repair at different calcination temperatures, respectively. As shown in Supplementary Fig. 15, the relationship between k_{obs} and the calcination temperatures was agreement with the volcano diagram, thus the optimal synthesis temperatures were determined to be 490 °C for NH_3 shear and 560 °C for thermal repair.

Based on the optimized experimental conditions, we further evaluated the photocatalytic activity of the prepared samples to elucidate the contribution of HSSA and highly polymerized molecular chains. As observed in Fig. 4b, c, pristine CN showed less than 60% removal of IMD in 9 min, with a k_{obs} of 0.056 min^{-1}. The catalytic activity of ACN that featured HSSA but with broken molecular chain structure was only slightly enhanced. Impressively, the NACN, with both HSSA and highly polymerized molecular chains, displayed the best IMD removal ability, achieving the largest k_{obs} of 0.405 min^{-1}, as 7.2 times higher than CN. Interestingly, while ANCN had a specific surface area comparable to that of NACN, its k_{obs} (0.068) was significantly lower. This implied that the highly polymerized molecular chains contributed more significantly to the photocatalytic activity compared to HSSA alone. As also perfectly substantiated by the higher IMD degradability of NCN only with highly polymerized molecular chains than ANCN. Meanwhile, the five photocatalysts' PMS consumption rates followed the same trend as their IMD degradation activity. NACN achieved a remarkable 90% PMS activation in 15 min (Fig. 4d). Moreover, the k_{obs} of IMD removal for NACN surpassed almost all reported photocatalysts (Fig. 4e and Supplementary Tables 8, 9). These results indicated that the synergistic effect of HSSA and highly polymerized molecular chains drastically boosted the carrier kinetic behaviors, leading to sufficiently activated PMS to sustainably generate reactive oxygen species for efficiently removing persistent pollutants.

The practical application of photocatalysts for water treatment critically depends on their interference resistance and reusability. Thus, we investigated the pollutant degradation performance of NACN under various harsh environmental conditions. In an initial examination, the NACN exhibited better IMD removal under acidic conditions than under alkaline conditions (Supplementary Fig. 16a), because $\cdot SO_4^-$ was likely to react with hydroxide to generate •OH, which processed a lower oxidation potential and shorter lifetime therefore impairing the IMD removal[60]. A similar trend was observed in the presence of co-existing ions (Supplementary Fig. 16b). Alkaline anions, such as HCO_3^- and CO_3^{2-}, inhibited IMD degradation. In contrast, the presence of acidic anions like SO_4^{2-} slightly promoted the degradation of IMD, while the enhancement of Cl^- and NO_3^- was much more significant. Reportedly, Cl^- can directly react with $\cdot SO_4^-$ and •OH to convert into •Cl, $\cdot Cl_2$, HClO, and ClO^-, which could efficiently oxidize various refractory pollutants[61].

The addition of natural organic matter (NOM) to the PC-PMS system significantly impacted the degradation dynamics (Supplementary Fig. 16c), as the NOM generally contains phenolic hydroxyl and carboxyl groups, which can interact with the photocatalyst and occupy active sites to hinder IMD removal[62]. Despite these potential interferences, NACN maintained excellent IMD removal from tap water and lake water (Supplementary Fig. 16d), with the water parameters shown in Supplementary Table 10. Importantly, the photocatalyst showed robust reusability with only a 5% decline of catalytic activity after ten cycles of operation (Fig. 4f). This slight decrease was possibly due to the partial loss of catalyst during the recovery process[63]. As depicted in Supplementary Fig. 17, the FTIR, XRD, and XPS spectra of

https://doi.org/10.1038/s41467-025-61185-3

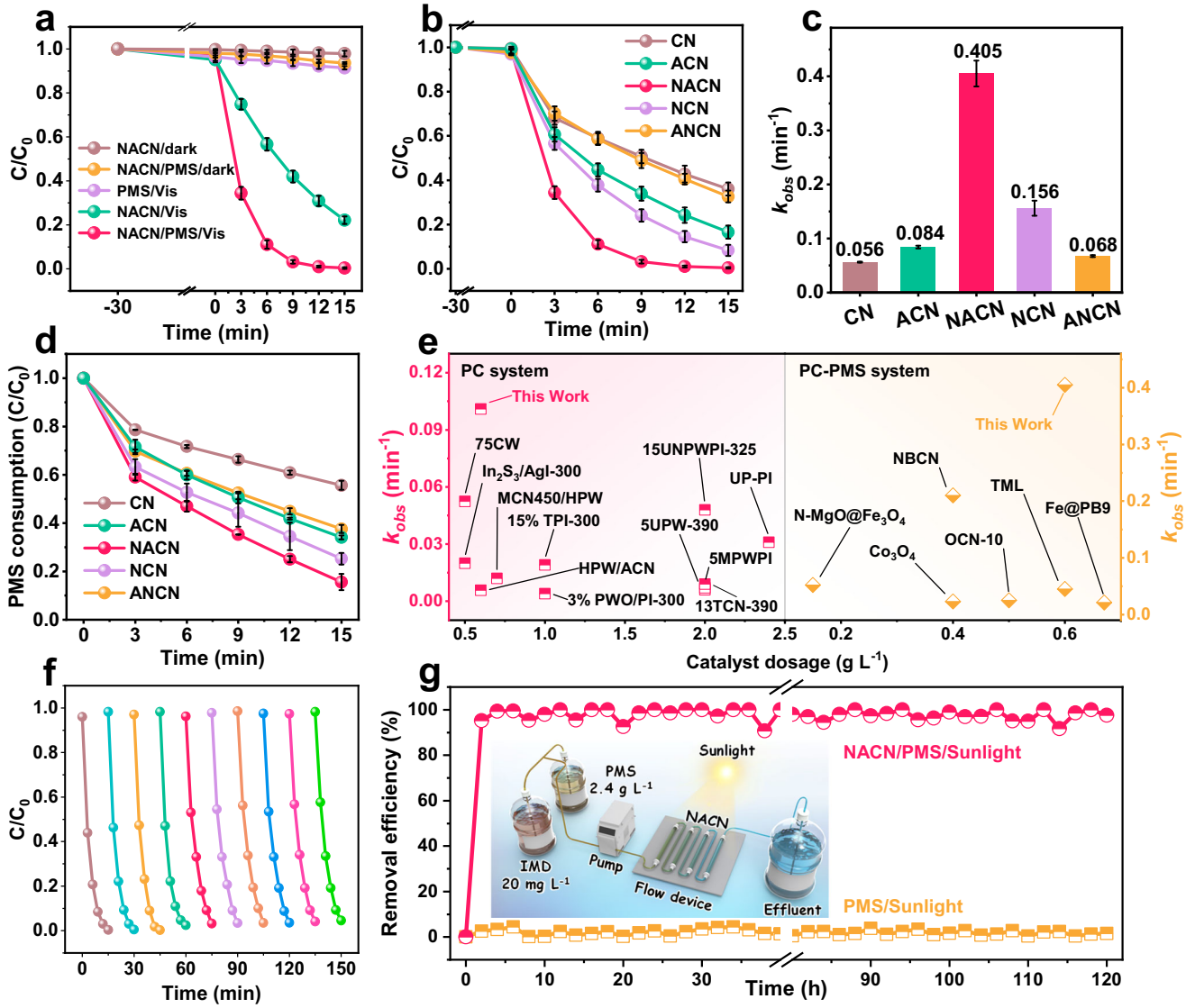

Fig. 4 | Evaluation of degradation performance of photocatalysts. a IMD degradation curves in various systems; **b** Kinetic curves of IMD removal by different photocatalysts and **c** corresponding rate constants k_{obs} in PC-PMS system. **d** PMS decomposition curves. The error bars represent the standard deviation derived from three repeated experiments. Reaction condition: [catalyst] = 0.06 g L^{-1}, [PMS] = 1.2 g L^{-1}, [IMD] = 10 mg L^{-1}, initial pH= 6.97 (if not adjusted), T = 298 K; **e** Comparison of the normalized k_{obs} of different reported works (The data are presented in Supplementary Tables 8, 9); **f** Cycling stability of the NACN under λ ≥ 420 nm visible light; **g** IMD removal efficiency in 20-day continuous flow reaction over NACN (Inset: The schematic diagram of custom-built continuous photo-flow device). Source data are provided as a Source Data file.

the catalysts before and after use remained nearly unchanged (Supplementary Fig. 17a–d), and no characteristic peaks of IMD appeared in the used catalyst, indicating the excellent structural stability of the catalyst and no IMD remained on the catalyst surface. Furthermore, the energy dispersive *X*-ray spectroscopy elemental mapping and EA results confirmed the comparable proportion of C and N elements in the catalysts before and after use (Supplementary Fig. 17e–g), suggesting no organic products were aggregated on the catalyst surface after the photoreaction. Subsequently, we used 2,6-di-tert-butyl-4-methylphenol (BHT) as polymerization inhibitor to suppress polymerization reactions[64,65]. As shown in Supplementary Fig. 17h, the BHT did not impede the IMD degradation, which excluded the IMD polymerization processes potentially occurring on the catalyst surface. The thermal gravimetric analysis revealed a similar pyrolysis process of the catalysts before and after use (Supplementary Fig. 17i), further supporting the absence of IMD residues or polymerization products on the catalyst surface. Based on these findings, we had sufficiently demonstrated that the removal of IMD was not achieved through the pollutant polymerization transfer pathway but through the conventional degradation and mineralization pathway.

To assess the long-term performance of NACN under real world conditions, we used a custom-built continuous photo-flow device for pollutants degradation under outdoor sunlight (Supplementary Fig. 18a). The IMD removal of NACN in the PC-PMS system remained consistently close to 100% throughout a continuous operating period of 20 days (total sunlight exposure time: 120 h), while PMS alone could not degrade IMD under sunlight (Fig. 4g). To visualize the pollutant removal process, we replaced IMD in the flow device by colored dyes as pollutants including rhodamine B and methyl orange. As shown in Supplementary Figs. 18b, c, and Supplementary Movies, the effluent from the device was colorless, demonstrating the great potential and durability of NACN for various pollutants removal in practical applications. Besides IMD and the dyes, NACN also achieved ultrahigh removal of other persistent pollutants, including phenol, thiacloprid,

https://doi.org/10.1038/s41467-025-61185-3

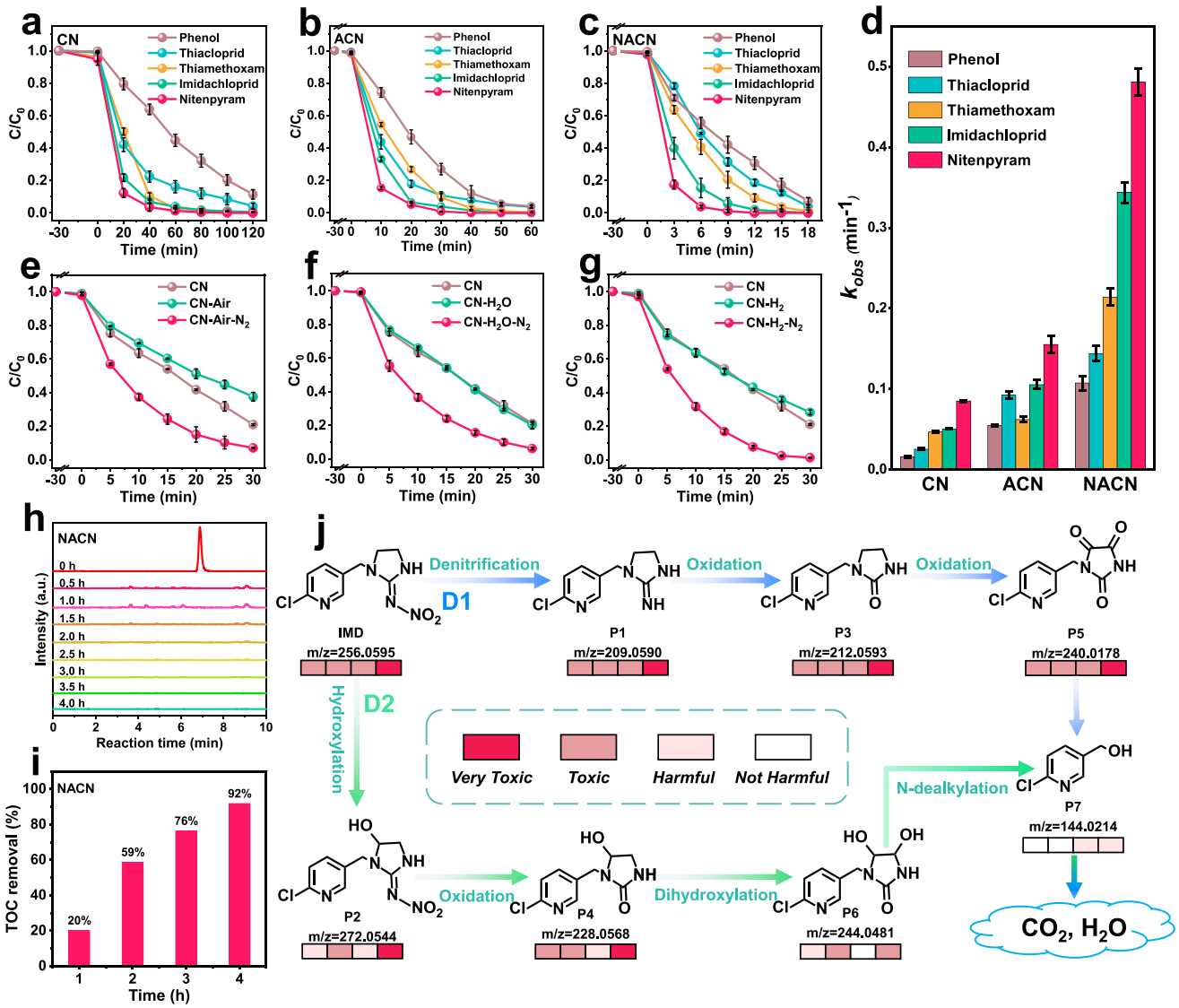

Fig. 5 | Universality of photocatalysts and pollutants mineralization. **a**–**c** Degradation curves of five pollutants for CN, ACN and NACN, respectively; **d** The corresponding k_{obs} values; **e**–**g** CN degradation curves after the first step of thermal shear treatment with air, water steam and hydrogen, respectively. The error bars represent the standard deviation derived from three repeated experiments; **h** The HPLC chromatograms of IMD and its intermediates; **i** TOC removal in IMD degradation process; **j** The degradation pathway analysis of IMD in the PC-PMS system, and toxic evolution of intermediates in the two degradation pathways evaluated by ECOSAR (LC_{50}/EC_{50}: half-lethal/effective concentration; Not harmful: $LC_{50}/EC_{50} > 100$ mg L^{-1}; Harmful: 100 mg $L^{-1} \geq LC_{50}/EC_{50} > 10$ mg L^{-1}; Toxic: 10 mg $L^{-1} \geq LC_{50}/EC_{50} > 1$ mg L^{-1}; Very Toxic: $LC_{50}/EC_{50} \leq 1$ mg L^{-1}; LC_{50}: Half lethal concentration; EC_{50}: Half effective concentration). The four different shades of red below each intermediate represent their acute and chronic toxicity to fish and daphnia, from left to right. Source data are provided as a Source Data file.

thiamethoxam, and nitenpyram (Fig. 5a–d). Even for the recalcitrant and highly toxic pollutant phenol, the corresponding k_{obs} of NACN still exceeded most of the reported catalysts (Supplementary Fig. 19 and Supplementary Table 11).

Thees results collectively demonstrated the photocatalyst had excellent interference resistance, reusability, and broad applicability of NACN for the efficient removal of various persistent pollutants under realistic conditions, highlighting its potential for sustainable environmental remediation.

To emphasize the universality of the shear and repair strategy for modulating carrier kinetic behaviors in g-C_3N_4 and thus further affecting the photocatalytic performance, NH_3 was replaced by other active atmospheres, including air (Fig. 5e), water steam (Fig. 5f), and hydrogen (Fig. 5g) in the first step of thermal shear. As expected, samples prepared only by thermal shear exhibited only slightly enhanced or even reduced photocatalytic activity. Inspirationally, after the subsequent thermal repair step, these samples displayed significantly improved degradation performance. Furthermore, when N_2 was replaced by inert argon atmosphere in the second step of thermal repair for ACN, the obtained sample had IMD degradability comparable to NACN (Supplementary Fig. 20). These results confirmed that the function of shearing and repairing the imine linkages was not limited to specific active and inert atmospheres.

Investigation of degradation mechanism

Achieving the complete mineralization and detoxification of persistent pollutants are crucial for practical water purification applications. High-performance liquid chromatography (HPLC) analysis revealed that the characteristic peak of IMD disappeared after 30 min, with the appearance of several intermediates. The characteristic peaks of all intermediates completely disappeared after 2 h (Fig. 5h). Moreover, NACN eliminated almost 90% of the total organic carbon in 4 h (Fig. 5i).

https://doi.org/10.1038/s41467-025-61185-3

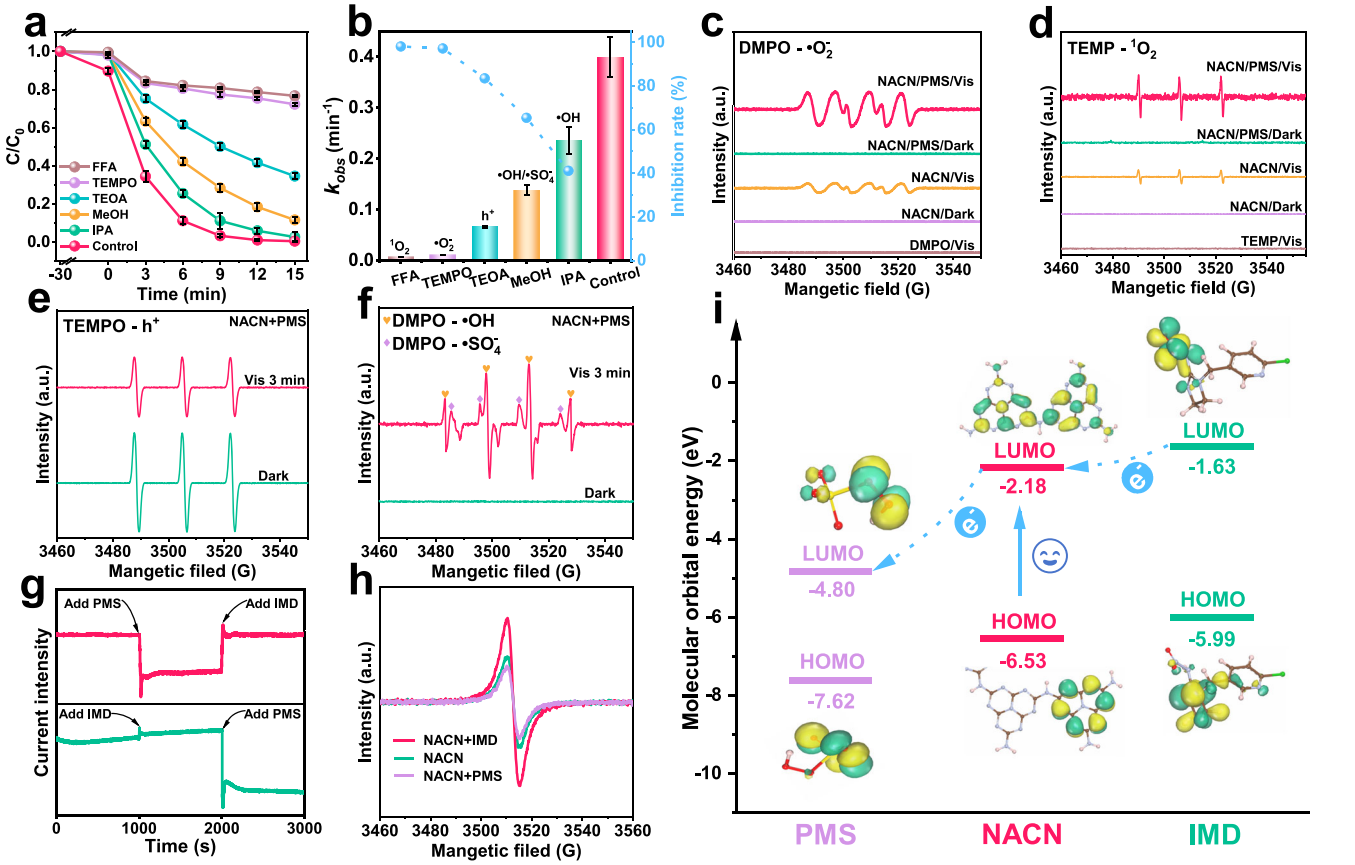

Fig. 6 | Evaluation of active species and possible mechanisms in PC-PMS system. a Comparison of degradation curves under different sacrificial agents; **b** Corresponding k_{obs} and inhibition rate. The error bars represent the standard deviation derived from three repeated experiments; **c**–**f** ESR spectra for active species in the presence of DMPO, TEMP and TEMPO in various systems; **g** Amperometric i-t curve measurements upon the addition of PMS and IMD using NACN as the working electrode; **h** ESR spectra upon addition of PMS and IMD, respectively; **i** Electron transfer pathways induced by external electric field. Source data are provided as a Source Data file.

This indicated that the degradation and mineralization of IMD occurred in parallel in the PC-PMS system, ultimately leading to completely mineralized into CO_2 and H_2O. Furthermore, the intermediates and possible pathways for IMD degradation were further investigated by ultrahigh performance liquid chromatography-mass spectrometry. Two possible IMD degradation pathways were proposed in Fig. 5j (see Supplementary Fig. 21 and Table 12). Simultaneously, the developmental toxicity of most intermediates derived from IMD estimated by the ECOSAR software was significantly reduced during the degradation process (see Supplementary Table 13), indicating that the degradation pathways of IMD were environmentally friendly and compatible.

To elucidate the mechanism behind the high degradation and mineralization efficiency of our photocatalyst, we conducted scavenging experiments using a series of sacrificial agents. Isopropanol (IPA), methanol (MeOH), triethanolamine (TEOA), furfuryl alcohol (FFA), and tetramethylpiperidine-nitrogen oxide (TEMPO) were employed to quench hydroxyl radicals (•OH), sulfate radicals ($•SO_4^-$), holes (h^+), superoxide radicals ($•O_2^-$), and singlet oxygen ($^1O_2$), respectively. Only a slight suppression effect was observed with the addition of IPA and MeOH (Fig. 6a, b), suggesting the conventional •OH and $•SO_4^-$ radicals did not play a crucial role in the degradation progress[66]. In contrast, the addition of TEOA, TEMPO and FFA significantly suppressed IMD removal, indicating the h^+, $•O_2^-$, and $^1O_2$ were the main active species involved in IMD degradation. The strongest inhibiting effect observed with TEMPO confirmed the predominant role of $^1O_2$ in the PC-PMS system.

ESR technology was subsequently utilized to directly detected the above active species generated during the degradation processes. When using 5,5-dimethyl-1-pyrroline N-oxide (DMPO) and 2,2,6,6-tetramethyl-4-piperidone (TEMP) as trapping agents, the ESR signals of $•O_2^-$ (Fig. 6c) and $^1O_2$ (Fig. 6d) were observed under light irradiation and significantly enhanced with the addition of PMS. Furthermore, we also observed a gradual weakening of the h^+ signal in the PC-PMS system (Fig. 6e). This indicated that $^1O_2$ was obtained by oxidation of $•O_2^-$ by h^+, which was a charge transfer process[67]. Additionally, the signals of •OH and $•SO_4^-$ were also observed in the PC-PMS system (Fig. 6f). These results were consistent with the reported generation of $^1O_2$ through the activation of $•SO_4^-$ and the situ conversion of •OH[68]. A detailed discussion of the conversion pathways for active species was given in Supplementary Discussion 12. These results indicated that the synergistic action of PMS and the photocatalyst generated multiple active species, which were ultimately converted to $^1O_2$ for supporting the highly efficient degradation of persistent pollutants.

To further understand the efficient $^1O_2$ generation mechanism, we investigated the charge transfer process among the pollutant, photocatalyst and PMS by combining experimental results and DFT calculations. As illustrated in Fig. 6g, the amperometry i − t curves of the electrochemical system with NACN-immobilized working electrode showed a sudden current drop upon PMS addition and a partial current rebound upon adding IMD. These observations indicated that IMD acted as an electron donor and PMS as an electron acceptor in the PC-PMS system[69]. Moreover, the ESR signal of the photocatalyst decreased

with the addition of PMS and increased with the addition of IMD (Fig. 6h). These results further supported the strong electron transfer among the electron-donating IMD, NACN photocatalyst and electron-withdrawing PMS.

DFT calculations were conducted to visualize the electron transfer mechanism among the IMD, NACN, and PMS. As observed in Fig. 6i, the LUMO of NACN (−2.18 eV) was closer in energy to the LUMO of IMD (−1.63 eV) than to the LUMO of PMS (−4.80 eV). This implied that electrons can be easily transferred from the LUMO of IMD to the LUMO of NACN and then to PMS, facilitating its activation. Based on these experimental and theoretical results, we proposed that the potential difference between the electron-donating pollutant and the electron-withdrawing PMS induced the generation of a microelectric field on the g-C_3N_4 surface. This microelectric field promoted the effective spatial separation of photogenerated carriers, significantly boosting photocatalytic PMS activation to sustainably generate $^1O_2$ for the efficient removal of various pollutants.

Discussion

In summary, we successfully synthesized ultrathin porous g-C_3N_4 nanosheets with HSSA and highly polymerized molecular chains using a versatile shear-repair strategy, which synergistically optimized the carrier kinetic behaviors, accelerating exciton dissociation and the subsequent separation and transfer of photogenerated carriers along the molecular chains. A critical point was the emergence of a microelectric field induced by the potential difference between the electron-donating pollutant and the electron-withdrawing PMS on the catalyst surface, which further boosted the spatial separation of photogenerated carriers, thereby favoring PMS activation to sustainably release $^1O_2$ for efficiently degrading and mineralizing various persistent pollutants even under harsh environmental conditions. This engineered photocatalyst exhibited superior stability, consistently maintaining near-100% pollutants' removal efficiency under real conditions of sunlight for 20 days of operation in a custom-built continuous photo-flow device. This work demonstrates the importance of balancing specific surface area and polymerization degree to engineer carrier kinetic behaviors, guiding the rational design of polymer-based photoelectric materials for sustainable environmental remediation and energy applications.

Methods

Chemicals and reagents

Detailed information is provided in the Supplementary information.

Preparation of CN

The CN catalyst was fabricated using thermal polymerization. Typically, 20.000 g of urea (CH_4N_2O) was placed in a 50 mL crucible with a lid and transferred to a muffle furnace. Then, the reagent was heated to 550 °C at a heating rate of 5 °C min^{-1} and stabilized for 4 h. After cooling to room temperature, 1.162 g (percent yields: 5.81%) yellow sample was obtained and used for subsequent experiments.

Preparation of ACN

0.500 g of CN powder was uniformly dispersed in an open crucible and placed in a tube furnace. The samples were calcined at different temperatures at a heating rate of 5 °C min^{-1} for 1 h under NH_3 atmosphere. The resulting samples were labeled as ACN-x (x = 470, 490, and 510, corresponding to calcination temperatures of 470, 490, and 510 °C, respectively). After cooling to room temperature, 0.185 g (percent yields: 37%) white sample (ACN) was obtained and used for subsequent experiments. In this work, ACN refers to ACN-490.

Preparation of NACN

0.200 g of ACN was placed in an open crucible and transferred to a tube furnace. The samples were calcined at different temperatures at a heating rate of 5 °C min^{-1} for 2 h under N_2 atmosphere. The obtained samples were named NACN-x (x = 540, 560, and 580, corresponding to calcination temperatures of 540, 560, and 580 °C, respectively). After cooling to room temperature, 0.192 g (percent yields: 96%) gray sample (NACN) was obtained and used for subsequent experiments. In this work, NACN refers to NACN-560.

Preparation of NCN and ANCN

NCN was obtained by directly calcining CN (0.200 g) at 560 °C for 2 h under N_2 atmosphere (0.195 g (percent yields: 97.5%) of sample available). Subsequently, 0.500 g NCN was calcined at 490 °C in an NH_3 atmosphere for 1 h to obtain ANCN (0.191 g (percent yields: 95.5%) of sample available). NCN and ANCN were used as control samples to evaluate the effect of different pyrolysis atmosphere orders on the structure and performance of catalysts.

Catalytic performance evaluation

All degradation experiments were carried out in a 50 mL reactor equipped with. a Xenon lamp (CEL-HXF300, Beijing Zhongjiao Jinyuan). The reactor was maintained at 25 ± 2 °C using circulating water and stirred during the experiments. Before irradiation, 30 mg of catalyst was first dispersed into 50 mL of IMD solution (10 ppm) and stirred (600 rpm) for 30 min in the dark to ensure adsorption-desorption equilibrium. Subsequently, 60 mg of PMS was rapidly added to the reactor while the Xenon lamp was turned on to initiate the reaction. Every 3 min, collected 1 mL suspension sample, filtered it with a 0.22 μm aqueous filter membrane, and immediately analyzed by HPLC (HPLC, Waters CAN ICES-1). The residual IMD was determined by HPLC at 270 nm using phosphoric acid and ultrapure water (1:1000 vol. ratio) as mobile phase.

Data availability

All study data are included in the article and Supplementary Information. Source data are provided with this paper.

References

1. Cao, S., Low, J., Yu, J. & Jaroniec, M. Polymeric photocatalysts based on graphitic carbon nitride. *Adv. Mater.* **27**, 2150–2176 (2015).
2. Xiao, Y. et al. Molecule self-assembly synthesis of porous few-layer carbon nitride for highly efficient photoredox catalysis. *J. Am. Chem. Soc.* **141**, 2508–2515 (2019).
3. Wang, X. et al. A metal-free polymeric photocatalyst for hydrogen production from water under visible light. *Nat. Mater.* **8**, 76–80 (2009).
4. Wang, Z. et al. Cobalt single atoms anchored on oxygen-doped tubular carbon nitride for efficient peroxymonosulfate activation: simultaneous coordination structure and morphology modulation. *Angew. Chem. Int. Ed.* **61**, 202202338 (2022).
5. Deng, J. et al. Advances of carbon nitride based atomically dispersed catalysts from single-atom to dual-atom in advanced oxidation process applications. *Coord. Chem. Rev.* **505**, 215693 (2024).
6. Lin, J. et al. Functional carbon nitride materials in photo-Fenton-like catalysis for environmental remediation. *Adv. Funct. Mater.* **32**, 2201743 (2022).
7. Wu, B. et al. Ultrathin porous carbon nitride bundles with an adjustable energy band structure toward simultaneous solar photocatalytic water splitting and selective phenylcarbinol oxidation. *Angew. Chem. Int. Ed.* **60**, 202013753 (2021).
8. Li, Q. et al. Shear stress triggers ultrathin-nanosheet carbon nitride assembly for photocatalytic H_2O_2 production coupled with selective alcohol oxidation. *J. Am. Chem. Soc.* **145**, 20837–20848 (2023).
9. Tan, C. et al. Recent advances in ultrathin two-dimensional nanomaterials. *Chem. Rev.* **117**, 5865 (2017).

10. Wu, B. et al. Ultrathin porous carbon nitride bundles with an adjustable energy band structure toward simultaneous solar photocatalytic water splitting and selective phenylcarbinol oxidation. *Angew. Chem. Int. Ed.* **60**, 4815–4822 (2021).
11. Guo, H. et al. Nitrogen-rich carbon dot-mediated n→π* electronic transition in carbon nitride for superior photocatalytic hydrogen peroxide production. *Adv. Funct. Mater.* **34**, 2402650 (2024).
12. Xu, Y. et al. Engineering built-in electric field microenvironment of CQDs/g-C_3N_4 heterojunction for efficient photocatalytic CO_2 reduction. *Adv. Sci.* **11**, 2403607 (2024).
13. Xiao, K., Giusto, P., Wen, L., Jiang, L. & Antonietti, M. Nanofluidic ion transport and energy conversion through ultrathin free-standing polymeric carbon nitride membranes. *Angew. Chem. Int. Ed.* **57**, 10123–10126 (2018).
14. Niu, P., Zhang, L., Liu, G. & Cheng, H.-M. Graphene-like carbon nitride nanosheets for improved photocatalytic activities. *Adv. Funct. Mater.* **22**, 4763–4770 (2012).
15. Wang, Y., Liu, L., Ma, T., Zhang, Y. & Huang, H. 2D graphitic carbon nitride for energy conversion and storage. *Adv. Funct. Mater.* **31**, 2102540 (2021).
16. Liang, Q., Li, Z., Huang, Z.-H., Kang, F. & Yang, Q.-H. Holey graphitic carbon nitride nanosheets with carbon vacancies for highly improved photocatalytic hydrogen production. *Adv. Funct. Mater.* **25**, 6885–6892 (2015).
17. Lan, H. et al. Hydrogen-induced defective crystalline carbon nitride with enhanced bidirectional charge migration for persulfate photoactivation. *ACS EST Eng.* **3**, 450 (2023).
18. Xie, P. et al. Oxo dicopper anchored on carbon nitride for selective oxidation of methane. *Nat. Commun.* **13**, 1375 (2022).
19. Yang, B. et al. Ultrathin porous carbon nitride nanosheets with well-tuned band structures via carbon vacancies and oxygen doping for significantly boosting H_2 production. *Appl Catal. B-Environ.* **314**, 121521 (2022).
20. Kang, Y. et al. Selective breaking of hydrogen bonds of layered carbon nitride for visible light photocatalysis. *Adv. Mater.* **28**, 6471–6477 (2016).
21. Zhang, G. et al. In-plane charge transport dominates the overall charge separation and photocatalytic activity in crystalline carbon nitride. *ACS Catal.* **12**, 4648–4658 (2022).
22. Zhang, G. et al. Breaking the limitation of elevated coulomb interaction in crystalline carbon nitride for visible and near-infrared light photoactivity. *Adv. Sci.* **9**, 2201677 (2022).
23. He, F. et al. Rejoint of carbon nitride fragments into multi-Interfacial order-disorder homojunction for robust photo-driven generation of H_2O_2. *Adv. Mater.* **36**, 2307490 (2024).
24. Huang J., et al. Modulating structural oxygen/crystallinity enables ambient cascade photo-upgrading of biomass saccharides to lactic acid. *Carbon Ener.* **7**, e675 (2025).
25. Chen, F. et al. Embedding electronic perpetual motion into single-atom catalysts for persistent Fenton-like reactions. *Proc. Natl. Acad. Sci. USA* **121**, e2314396121 (2024).
26. Liu, Y. et al. Single-crystalline ultrathin 2D porous nanosheets of chiral metal–organic frameworks. *J. Am. Chem. Soc.* **143**, 3509–3518 (2021).
27. Yang, Z. et al. Defect-repaired g-C_3N_4 nanosheets: elevating the efficacy of sonodynamic cancer therapy through enhanced charge carrier migration. *Angew. Chem. Int. Ed.* **63**, e202401758 (2024).
28. Yang, S. et al. Exfoliated graphitic carbon nitride nanosheets as efficient catalysts for hydrogen evolution under visible light. *Adv. Mater.* **25**, 2452–2456 (2013).
29. Lotsch, B. V. et al. Unmasking melon by a complementary approach employing electron diffraction, solid-state NMR spectroscopy, and theoretical calculations-structural characterization of a carbon nitride polymer. *Chem. Eur. J.* **13**, 4969–4980 (2007).
30. Fina, F., Callear, S. K., Carins, G. M. & Irvine, J. T. S. Structural investigation of graphitic carbon nitride via XRD and neutron diffraction. *Chem. Mater.* **27**, 2612–2618 (2015).
31. Wu, J. et al. Regulating polymerization in graphitic carbon nitride to improve photocatalytic activity. *Chem. Mater.* **31**, 9188–9199 (2019).
32. Peng, G., Albero, J., Garcia, H. & Shalom, M. A water-splitting carbon nitride photoelectrochemical cell with efficient charge separation and remarkably low onset potential. *Angew. Chem. Int. Ed.* **57**, 15807–15811 (2018).
33. Akaike, K., Aoyama, K., Dekubo, S., Onishi, A. & Kanai, K. Characterizing electronic structure near the energy gap of graphitic carbon nitride based on rational interpretation of chemical analysis. *Chem. Mater.* **30**, 2341–2352 (2018).
34. Hu, E. et al. Cyano-functionalized graphitic carbon nitride with adsorption and photoreduction isosite achieving efficient uranium extraction from seawater. *Adv. Funct. Mater.* **34**, 2312215 (2024).
35. Zhang, P. et al. Heteroatom dopants promote two-electron O_2 reduction for photocatalytic production of H_2O_2 on polymeric carbon nitride. *Angew. Chem. Int. Ed.* **59**, 16209–16217 (2020).
36. Ran, J. et al. Metal-free 2D/2D phosphorene/g-C_3N_4 Van der Waals heterojunction for highly enhanced visible-light photocatalytic H_2 production. *Adv. Mater.* **30**, 1800128 (2018).
37. Feng, B. et al. Tailored exfoliation of polymeric carbon nitride for photocatalytic H_2O_2 production and CH_4 valorization mediated by O_2 activation. *Angew. Chem. Int. Ed.* **63**, e202401884 (2024).
38. Zhao, D. et al. Synergy of dopants and defects in graphitic carbon nitride with exceptionally modulated band structures for efficient photocatalytic oxygen evolution. *Adv. Mater.* **31**, 1903545 (2019).
39. Liang, Y. et al. Covalent hybrid of spinel manganese–cobalt oxide and graphene as advanced oxygen reduction electrocatalysts. *J. Am. Chem. Soc.* **134**, 3517–3523 (2012).
40. Yang, M. et al. Photocatalytic cyclization of nitrogen-centered radicals with carbon nitride through promoting substrate/catalyst interaction. *Nat. Commun.* **13**, 4900 (2022).
41. Jia, Y. et al. Identification of active sites for acidic oxygen reduction on carbon catalysts with and without nitrogen doping. *Nat. Catal.* **2**, 688–695 (2019).
42. Zhang, G. et al. Formation of Bi_2WO_6 bipyramids with vacancy pairs for enhanced solar-driven photoactivity. *Adv. Funct. Mater.* **25**, 3726–3734 (2015).
43. Guan, M. et al. Vacancy associates promoting solar-driven photocatalytic activity of ultrathin bismuth oxychloride nanosheets. *J. Am. Chem. Soc.* **135**, 10411–10417 (2013).
44. Liu, X., Zhou, K., Wang, L., Wang, B. & Li, Y. Oxygen vacancy clusters promoting reducibility and activity of ceria nanorods. *J. Am. Chem. Soc.* **131**, 3140–3141 (2009).
45. Hestand, N. J. et al. Extended-charge-transfer excitons in crystalline supramolecular photocatalytic scaffolds. *J. Am. Chem. Soc.* **138**, 11762–11774 (2016).
46. Li, C. et al. Covalent organic frameworks with high quantum efficiency in sacrificial photocatalytic hydrogen evolution. *Nat. Commun.* **13**, 2357 (2022).
47. Shi, Y. et al. Van der Waals gap-rich BiOCl atomic layers realizing efficient, pure-water CO_2-to-CO photocatalysis. *Nat. Commun.* **12**, 5923 (2021).
48. Liao, G. et al. Semiconductor polymeric graphitic carbon nitride photocatalysts: the "holy grail" for the photocatalytic hydrogen evolution reaction under visible light. *Energy Environ. Sci.* **12**, 2080–2147 (2019).
49. Wang, X. et al. Induced dipole moments in amorphous ZnCdS catalysts facilitate photocatalytic H_2 evolution. *Nat. Commun.* **15**, 2600 (2024).
50. Zhu, Y. et al. A [001]-oriented hittorf's phosphorus nanorods/polymeric carbon nitride heterostructure for boosting wide-spectrum-

responsive photocatalytic hydrogen evolution from pure water. *Angew. Chem. Int. Ed.* **59**, 868–873 (2020).
51. Sun, T. et al. Engineering the electronic structure of MoS_2 nanorods by N and Mn dopants for ultra-efficient hydrogen production. *ACS Catal.* **8**, 7585–7592 (2018).
52. Liu, B. et al. Regulating the transfer of photogenerated carriers for photocatalytic hydrogen evolution coupled with furfural synthesis. *ACS Nano* **18**, 17939–17949 (2024).
53. Guo, Y. et al. Reinforced interfacial Cd—Se bond coupling photocatalytic hydrogen evolution with pyruvic acid synthesis. *Adv. Energy Mater.* **14**, 2401285 (2024).
54. Liu, Y., Cullen, D. A. & Lian, T. Slow auger recombination of trapped excitons enables efficient multiple electron transfer in CdS–Pt nanorod heterostructures. *J. Am. Chem. Soc.* **143**, 20264–20273 (2021).
55. Xu, X. et al. Full-spectrum responsive naphthalimide/perylene diimide with a giant internal electric field for photocatalytic overall water splitting. *Angew. Chem. Int. Ed.* **63**, e202308597 (2024).
56. Bie, C. et al. A bifunctional CdS/MoO_2/MoS_2 catalyst enhances photocatalytic H_2 evolution and pyruvic acid synthesis. *Angew. Chem., Int. Ed.* **61**, e202212045 (2022).
57. Godin, R., Wang, Y., Zwijnenburg, M. A., Tang, J. & Durrant, J. R. Time-resolved spectroscopic investigation of charge trapping in carbon nitrides photocatalysts for hydrogen generation. *J. Am. Chem. Soc.* **139**, 5216–5224 (2017).
58. Zhu, X. et al. Imidacloprid crystal polymorphs for disease vector control and pollinator protection. *J. Am. Chem. Soc.* **143**, 17144–17152 (2021).
59. Caserto, J. S. et al. Ingestible hydrogel microparticles improve bee health after pesticide exposure. *Nat. Sustain.* **7**, 1441–1451 (2024).
60. Qin, F. et al. Catalyst-free photochemical activation of peroxymonosulfate in xanthene-rich systems for Fenton-like synergistic decontamination: efficacy of proton transfer process. *Angew. Chem. Int. Ed.* **62**, e202300256 (2023).
61. Zhong, Y. et al. Ultrathin BiOCl-OV/CoAl-LDH S-scheme heterojunction for efficient photocatalytic peroxymonosulfate activation to boost Co (IV)=O generation. *Water Res.* **258**, 121774 (2024).
62. Guan, Y.-H. et al. Efficient degradation of atrazine by magnetic porous copper ferrite catalyzed peroxymonosulfate oxidation via the formation of hydroxyl and sulfate radicals. *Water Res.* **47**, 5431–5438 (2013).
63. Wang, B. et al. A site distance effect induced by reactant molecule matchup in single-atom catalysts for Fenton-like reactions. *Angew. Chem. Int Ed.* **61**, e202207268 (2022).
64. Feng, C. & Loh, T.-P. Copper-catalyzed olefinic trifluoromethylation of enamides at room temperature. *Chem. Sci.* **3**, 3458–3462 (2012).
65. Chen Z. et al. Organic carbon transfer process in advanced oxidation systems for water clean-up. *Nat. Water* **3**, 334–344 (2025).
66. Zhou, X. et al. Identification of Fenton-like active Cu sites by heteroatom modulation of electronic density. *Proc. Natl. Acad. Sci. USA* **119**, e2119492119 (2022).
67. Xu, M., Wang, R., Fu, H., Shi, Y. & Ling, L. Harmonizing the cyano-group and Na to enhance selective photocatalytic O_2 activation on carbon nitride for refractory pollutant degradation. *Proc. Natl. Acad. Sci. USA* **121**, e2318787121 (2024).
68. Wang, A. et al. Enhanced and synergistic catalytic activation by photoexcitation driven S-scheme heterojunction hydrogel interface electric field. *Nat. Commun.* **14**, 6733 (2023).
69. Guo, J. et al. Fenton-like activity and pathway modulation via single-atom sites and pollutants comediates the electron transfer process. *Proc. Natl. Acad. Sci. USA* **121**, e2313387121 (2024).

Acknowledgements

This study was mainly supported by the National Natural Science Foundation of China (Grant No. 22308223), the High-level Talents launching Project (RCZK202328), and Xinjiang Uygur Autonomous Region Tianchi Talent Introduction Program (Young Doctor) for Bin Yang. This study was also supported by the National Natural Science Foundation of China (Grant No. U1703351, 52073179, 22308336), Tianshan Talent Support Program for Xin Jia, and the Program of Introducing Talents of Discipline to Universities (D20018). The authors would like to thank Shiyanjia Lab (www.shiyanjia.com) for the XPS analysis.

Author contributions

H.L. and B.Y. conceived the experiments, analyzed the data and wrote the paper with inputs from all authors. X.J. and B.Y. supervised the project. H.L. fabricated the materials and carried out the main experiments. J.L. and G.F.L. analyzed experimental data. B.Y.H. made the theoretical analyses. H.L., B.Y., J.L., R.R., and X.J. together analyzed the original data and prepared writing review & editing. All authors joined in to review and edit the paper.

Competing interests

The authors declare no competing interests.

Additional information

Supplementary information The online version contains supplementary material available at https://doi.org/10.1038/s41467-025-61185-3.

Correspondence and requests for materials should be addressed to Bin Yang, Jun Li or Xin Jia.

Peer review information *Nature Communications* thanks Chang-Gu Lee and the other, anonymous, reviewer(s) for their contribution to the peer review of this work. A peer review file is available.

Reprints and permissions information is available at http://www.nature.com/reprints

Publisher's note Springer Nature remains neutral with regard to jurisdictional claims in published maps and institutional affiliations.

Open Access This article is licensed under a Creative Commons Attribution-NonCommercial-NoDerivatives 4.0 International License, which permits any non-commercial use, sharing, distribution and reproduction in any medium or format, as long as you give appropriate credit to the original author(s) and the source, provide a link to the Creative Commons licence, and indicate if you modified the licensed material. You do not have permission under this licence to share adapted material derived from this article or parts of it. The images or other third party material in this article are included in the article's Creative Commons licence, unless indicated otherwise in a credit line to the material. If material is not included in the article's Creative Commons licence and your intended use is not permitted by statutory regulation or exceeds the permitted use, you will need to obtain permission directly from the copyright holder. To view a copy of this licence, visit http://creativecommons.org/licenses/by-nc-nd/4.0/.

© The Author(s) 2025